

The Mass Distribution of Quasars in Optical Time-domain Surveys

Mouyuan Sun,^{1*}

¹*Department of Astronomy, Xiamen University, Xiamen, Fujian 361005, China*

Accepted XXX. Received YYY; in original form ZZZ

ABSTRACT

The determination of supermassive black hole (SMBH) masses is the key to understanding the host galaxy build-up and the SMBH mass assembly histories. The SMBH masses of non-local quasars are frequently estimated via the single-epoch virial black-hole mass estimators, which may suffer from significant biases. Here we demonstrate a new approach to infer the mass distribution of SMBHs in quasars by modelling quasar UV/optical variability. Our inferred black hole masses are systematically smaller than the virial ones by 0.3 ~ 0.6 dex; the ~ 0.3 dex offsets are roughly consistent with the expected biases of the virial black-hole mass estimators. In the upcoming time-domain astronomy era, our methodology can be used to constrain the cosmic evolution of quasar mass distributions.

Key words: quasars: general – quasars: supermassive black holes – accretion, accretion discs

1 INTRODUCTION

The mass distribution of supermassive black holes (SMBHs) in galaxy centres is vital for our understanding of their mass assembly histories, the active galactic nucleus (AGN) feedback energy budget, and the evolution of host galaxies. For distant AGNs (including quasars, i.e., luminous AGNs with broad emission lines), their SMBH masses (M_{BH}) are often estimated via the reverberation mapping method (Blandford & McKee 1982) and its simplified version, the single-epoch virial black-hole mass estimators (for a review, see, e.g., Shen 2013). The two methods are built upon the assumption that the broad emission-line regions (BLRs), which are photoionized by the central engine and emit broad emission lines, are virialized. The virial mass estimators are calibrated (e.g., Onken et al. 2004) with respect to the famous $M_{\text{BH}}-\sigma$ relation (Ferrarese & Merritt 2000; Gebhardt et al. 2000) under the assumption that AGNs have similar virial factors. It has been shown that the virial black hole mass ($M_{\text{BH,vir}}$) has substantial intrinsic uncertainties ($\gtrsim 0.4$ dex) and suffers from systematic biases ($\gtrsim 0.3$ dex; see, e.g., Shen & Kelly 2010). Ongoing (e.g., Du et al. 2016; Homayouni et al. 2020; Yu et al. 2022) and future reverberation mapping campaigns may considerably improve the accuracy of $M_{\text{BH,vir}}$ by monitoring a large quasar sample and modelling their BLR structures (e.g., Pancoast et al. 2014; Li et al. 2021).

In the upcoming time-domain era of astronomy, scaling relations between M_{BH} and AGN variability properties are often proposed to estimate M_{BH} since AGN variability is unambiguous in various wavelengths. Previous studies often focus on the X-ray excess variance and find that the correspond-

ing mass estimation precision is comparable to the reverberation mapping method (e.g., Zhou et al. 2010; Kelly et al. 2013). Some works take an alternative approach by adopting the M_{BH} -galaxy total stellar mass (M_*) scaling relations to model the ensemble X-ray variability and constrain the mass distribution of AGNs in deep X-ray surveys (e.g., Georgakakis, Papadakis, & Paolillo 2021). In the next decade, the Legacy Survey of Space and Time (LSST) of the Vera C. Rubin Observatory will comprehensively measure AGN variability in the optical bands (e.g., Brandt et al. 2018). While several studies have discussed the possibility to use optical variability to estimate M_{BH} (e.g., Kelly & Shen 2013; Sun et al. 2020; Burke et al. 2021), the validity of such a method has not yet been well demonstrated.

In this study, we aim to constrain the mass distribution of quasars by modelling their optical structure functions measured from the Sloan Digital Sky Survey (SDSS) Stripe 82 (S82; MacLeod et al. 2012) and the Panoramic Survey Telescope and Rapid Response System Survey (Pan-STARRS; Chambers et al. 2016; Flewelling et al. 2020) light curves. The manuscript is formatted as follows. In Section 2, we present the observed quasar variability. In Section 3, we introduce our quasar variability forward modelling procedures. In Section 4, we show the modelling results. Summary and future prospects are made in Section 5.

2 OBSERVATIONS

Following Suberlak, Ivezić, & MacLeod (2021), we use the SDSS S82 quasar light curves and Pan-STARRS observations to explore quasar variations on observed-frame timescales up to 15 years. The SDSS S82 quasar light

* E-mail: msun88@xmu.edu.cn

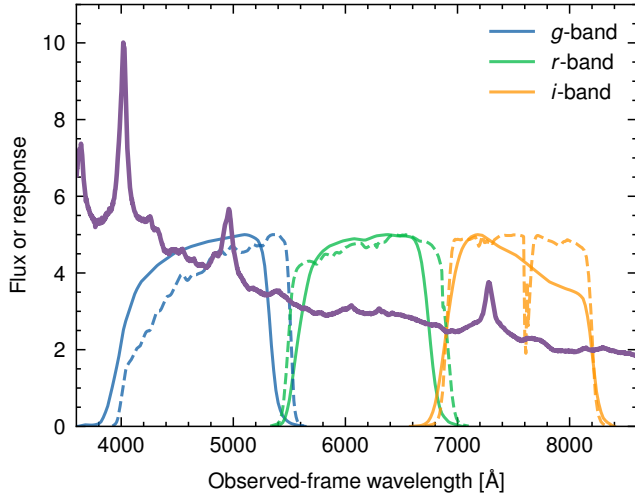


Figure 1. Transmission curves of SDSS (solid curves) and Pan-STARRS (dashed curves) *gri* bands. The purple curve represents the SDSS composite spectrum at redshift $z = 1.6$. Contamination due to strong UV emission lines, e.g., C IV and Ly α , are negligible in our studies.

curves (each light curve typically contains 40 data points) are downloaded from https://faculty.washington.edu/ivezic/cmacleod/qso_dr7/Southern.html. Then, we cross-match each SDSS S82 quasar with the Pan-STARRS second data release (<https://catalogs.mast.stsci.edu/panstarrs/>; each light curve typically has twelve observations) to extend the light-curve duration.

We focus on the 2114 quasars at redshift $1.4 < z < 1.8$ because the redshift distribution of our quasar sample peaks at this range. The median redshift for the selected quasars is 1.6. We cross-match the selected quasars with the quasar property catalogue of Shen et al. (2011) to obtain their bolometric luminosities (L_{bol}) and $M_{\text{BH,vir}}$; our conclusions remain unchanged if we use the updated quasar property catalogue of Wu & Shen (2022). The selected quasars are divided into five $\log L_{\text{bol}}$ bins; each bin has the same number of quasars. Hence, the $\log L_{\text{bol}}$ bins are defined as follows: [45.79, 45.97], [45.97, 46.10], [46.10, 46.25], [46.25, 46.47], and [46.47, 46.77].

The SDSS S82 data have five bands, i.e., *ugriz*. The Pan-STARRS survey has *grizy* filters. The SDSS *gri* and Pan-STARRS *gri* have similar filter response curves; the SDSS *z* differ significantly from Pan-STARRS *z*. Hence, we focus on the SDSS and Pan-STARRS *gri* light curves. For the redshift ranges of our selected quasars, according to the SDSS composite spectrum (Vanden Berk et al. 2001), the *r*-band flux is emission-line free; *g* and *i* fluxes have weak inevitable contamination due to Mg II and C III] (Figure 1). We assume that such contamination is negligible (see, e.g., MacLeod et al. 2012) in our subsequent analysis.

Following Suberlak, Ivezić, & MacLeod (2021), we use the SDSS S82 standard stars v4.2 of Thanjavur et al. (2021) to find the difference (δm_{diff}) of the SDSS and Pan-STARRS magnitudes at each band as a function of the SDSS $g - r$ colour index,

$$\delta m_{\text{diff}} = A + B(m_g - m_r), \quad (1)$$

where m_g and m_r are the apparent magnitudes in SDSS *g*

Table 1. The normalization (10^s) and intrinsic scatter (σ_{int}) of the $M_{\text{BH}}-M_{\star}$ relation

Case	10^s	σ_{int}
1	500	0.3
2	500	0.6
3	500	1.2
4	1000	0.3
5	1000	0.6
6	1000	1.2
7	2000	0.3
8	2000	0.6
9	2000	1.2
10	4000	0.3
11	4000	0.6
12	4000	1.2
13	8000	0.3
14	8000	0.6
15	8000	1.2

and *r* bands, respectively. We use the $g - r$ colour index rather than the $g - i$ one because the *r* band is emission-line free (Figure 1). For *g*, *r*, and *i* bands, we find that $A = 0.01836$, 0.0009, and 0.0199, and $B = 0.154$, 0.001, and 0.008, respectively. Then, we use the empirical correction of Eq. 1 and quasar $g - r$ colour indexes to convert the observed Pan-STARRS magnitudes into the corresponding SDSS magnitudes and construct merged quasar light curves.

We adopt the SDSS S82 and Pan-STARRS merged light curves to calculate the squared structure functions (SF^2) which measure the statistical variance of quasar magnitude fluctuations (Δm) at a given band and a fixed rest-frame time separation (Δt). We consider twenty-two Δt which are evenly spaced between rest-frame 1 day and 2,000 days in logarithmic space. For each Δt , the corresponding variability amplitude of Δm is calculated via the squared normalized average absolute deviation (squared NAAD),

$$\text{SF}^2(\Delta t) \equiv \sigma_{\text{NAAD}}^2 = \frac{\pi}{2} \times \left(\overline{|\Delta m - \overline{\Delta m}|} \right)^2, \quad (2)$$

where $\overline{\Delta m}$ represents the average value of Δm ; the factor, $\pi/2$, ensures that σ_{NAAD}^2 is identical to the variance if the distribution of Δm is perfectly Gaussian. We do not subtract Δm fluctuations due to magnitude measurement uncertainties. Hence, on very short Δt (e.g., ~ 1 day), σ_{NAAD}^2 traces the measurement uncertainties of Δm ; on timescales of ≥ 10 days (in rest-frame), σ_{NAAD}^2 probes quasar intrinsic variability.

The observed squared structure functions are shown in Figure 2. As shown in previous SDSS S82 studies (e.g., MacLeod et al. 2012; Suberlak, Ivezić, & MacLeod 2021), the squared structure functions increase with Δt and anti-correlate with wavelengths and quasar luminosities, which agree well with the Corona Heated Accretion disc Reprocessing (CHAR) model predictions (Sun et al. 2020). It has been shown that the CHAR model can reproduce the ensemble structure functions of SDSS S82 light curves (Sun et al. 2020).

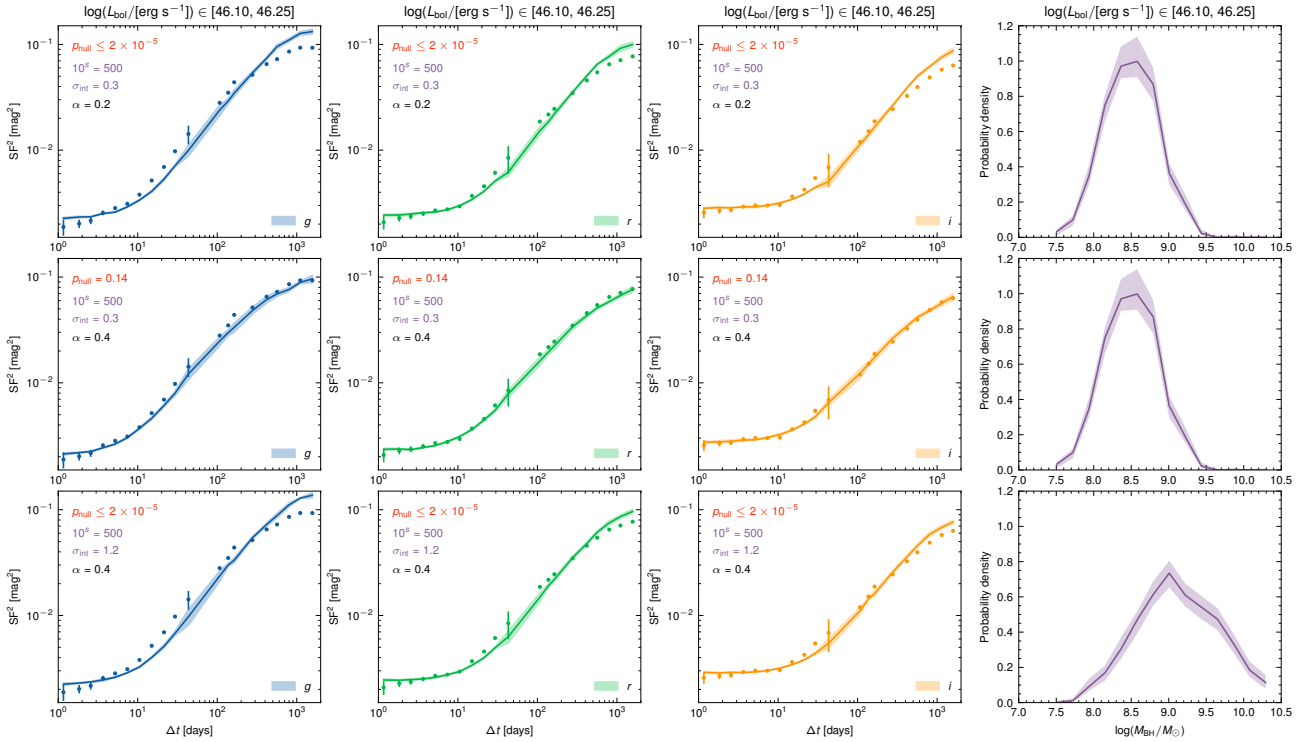


Figure 2. An illustration of the observed (points) squared structure functions versus the model (solid curves) and 1σ uncertainties (i.e., shaded regions) for models with two different α values or M_{BH} distributions (shown in the fourth column). The M_{BH} distributions are controlled by 10^s and σ_{int} . The upper, middle, and bottom rows correspond to models with $[10^s = 500, \sigma_{\text{int}} = 0.3 \text{ dex}, \alpha = 0.2]$, $[10^s = 500, \sigma_{\text{int}} = 0.3 \text{ dex}, \alpha = 0.4]$, and $[10^s = 500, \sigma_{\text{int}} = 1.2 \text{ dex}, \alpha = 0.4]$, respectively. The first, second, and third columns represent the results for g , r , and i bands, respectively. Panels in the same column have exactly the same observed squared structure functions whose error bars are estimated via $1/N_{\text{p}}$, where N_{p} is the number of data pairs in each Δt bin; error bars are smaller than point sizes in most Δt bins. The p_{null} value is calculated by simultaneously considering the observed squared structure functions of all five luminosity bins and three bands; hence, p_{null} is the same in each row. The model with $[10^s = 500, \sigma_{\text{int}} = 0.3 \text{ dex}, \alpha = 0.4]$ fits the observations better than other two models with either different α or σ_{int} . Note that the results in this figure are for the luminosity bin $46.10 \leq \log(L_{\text{bol}}/[\text{erg s}^{-1}]) < 46.25$; the results for other four luminosity bins are presented in Appendix A.

3 MODELLING THE OBSERVED STRUCTURE FUNCTIONS

We use the CHAR model (for the implemented physics, please refer to Sun et al. 2020) to generate mock light curves; then, we compare the squared structure functions of the mock data with the observed ones. SMBHs are assumed to be Schwarzschild black holes, and the inner and outer boundaries of the accretion discs are $3 R_{\text{S}}$ and $3000 R_{\text{S}}$ (where R_{S} is the Schwarzschild radius), respectively. To use the CHAR model, we have to assign four parameters, namely, L_{bol} , M_{BH} , the dimensionless viscosity parameter α , and the variability amplitude (δ_{mc}) of the magnetic fluctuations in the CHAR model. We consider two cases for α , i.e., $\alpha = 0.2$ and $\alpha = 0.4$ (e.g., King, Pringle, & Livio 2007). We also assume that δ_{mc} is independent of M_{BH} or L_{bol} , which are the remaining two parameters.

Different from our previous study (Sun et al. 2020, which only uses SDSS S82 light curves and probes rest-frame timescales of $\Delta t \lesssim 500$ days), we now do not fix the model M_{BH} to $M_{\text{BH, vir}}$ since the latter suffers from various biases and has substantial uncertainties (for a review, see, e.g., Shen 2013). Instead, we take a forward-modelling approach and consider the correlation between M_{BH} and the total stellar mass (M_{\star}) of their host galaxies (e.g., Sun et al. 2015; Li et

al. 2021, and references therein), i.e.,

$$\log(M_{\text{BH}}/M_{\odot}) = \log(M_{\star}/M_{\odot}) - s, \quad (3)$$

with the intrinsic scatter follows a log-normal distribution, whose standard deviation is σ_{int} . We assume that the probability density function of M_{\star} is a summation of two Schechter functions, and we adopt the continuity model parameters (at redshift $z = 1.6$) obtained by Leja et al. (2020, see their appendix B). For the value of s (i.e., the normalization of the scaling relation), we consider five cases, i.e., $10^s = 500, 1000, 2000, 4000,$ and 8000 , respectively. For σ_{int} , we explore three values, i.e., $\sigma_{\text{int}} = 0.3 \text{ dex}, 0.6 \text{ dex},$ and 1.2 dex , respectively. That is, we consider $5 \times 3 = 15$ cases (for a summary, see Table 1). It should be noted that this approach is equivalent to assuming a specific intrinsic distribution of $\log M_{\text{BH}}$, which is a convolution of the summation of two Schechter functions and a normal distribution (whose mean and standard deviation are s and σ_{int} , respectively). Due to various selection effects, the $\log M_{\text{BH}}$ distribution of the observed quasars are different from the intrinsic one. Below, we will simulate the detectable mock quasars by applying selection cuts to the intrinsic $\log M_{\text{BH}}$ distribution.

Our mock light-curve simulation process is similar to that of Georgakakis, Papadakis, & Paolillo (2021). First, we randomly sample mock galaxies (with M_{\star}) according to the

galaxy stellar mass function of [Leja et al. \(2020\)](#). Second, for each mock galaxy, we assign an SMBH with M_{BH} according to Eq. 3. Third, we assume the Eddington ratio distribution of AGNs follows the Schechter function, i.e.,

$$\frac{dt}{d \log \lambda_{\text{Edd}}} \propto \left(\frac{\lambda_{\text{Edd}}}{\lambda_{\text{Edd,cut}}} \right)^{-\gamma} \exp(-\lambda_{\text{Edd}}/\lambda_{\text{Edd,cut}}) \quad , \quad (4)$$

where λ_{Edd} represents the Eddington ratio; the slope γ and $\lambda_{\text{Edd,cut}}$ are fixed¹ to be 0.2 and 0.4 ([Jones et al. 2016](#)), respectively. The lower limit of $\log \lambda_{\text{Edd}}$ is fixed to be -4 (i.e., much smaller than the observed $\log \lambda_{\text{Edd}}$ for quasars) for Case 1; the lower limits of λ_{Edd} for other cases are adjusted to ensure that their corresponding mean values of $\log L_{\text{bol}}$ are identical to that of Case 1. Note that our models can reproduce the observed quasar luminosity function. Fourth, we calculate the corresponding bolometric luminosity (L_{bol}) and convert it into the 3000 continuum luminosity (L_{3000} , i.e., λL_{λ} at $\lambda = 3000$) by adopting a constant bolometric correction² of 5 (whose intrinsic scatter follows a log-normal distribution with the standard deviation of 0.3), and obtain the corresponding i -band apparent magnitude (m_i) and the FWHM of Mg II (see Eq. 8 in [Shen et al. 2011](#)). Fifth, we select mock quasars with m_i brighter than 20.3 mag and the FWHM of Mg II larger than 10^3 km s^{-1} (hereafter the “detectable” mock quasars); the m_i limit of 20.3 mag corresponds to the 95-th percentile of the m_i distribution of the 2114 quasars in Section 2. Sixth, for each luminosity bin introduced in Section 2, we randomly select the same number of mock quasars whose L_{bol} (i.e., $5L_{3000}$) fall into the luminosity bin. Seventh, for each selected mock quasar, we use its L_{bol} and M_{BH} and the CHAR model to calculate their multi-wavelength light curves. The mock light curves share the same sampling pattern as real observations. In this procedure, δ_{mc} (i.e., the magnetic fluctuation amplitude) is unknown and should be determined according to observations. To save the computation time, we calculate the mock light curves for a given δ_{mc} (denoted as $\delta_{\text{mc},0}$), which is independent of L_{bol} , M_{BH} , and α . The model ensemble squared structure functions for other choices of δ_{mc} can be obtained by multiplying the factor $c = (\delta_{\text{mc}}/\delta_{\text{mc},0})^2$ with the model squared ensemble structure functions for $\delta_{\text{mc},0}$. Finally, we calculate the model ensemble squared structure functions (SF_{mock}^2) with the same methodology aforementioned. We repeat the calculation 64 times to estimate the statistical dispersion of a squared structure function.

We use the following statistic for each luminosity bin and each band to fit the model against the data and determine δ_{mc} , i.e.,

$$\chi_{\text{P,L},\lambda}^2 = \sum \frac{(\log SF_{\text{obs}}^2 - \log(c \times SF_{\text{mock}}^2 + SF_{\text{err}}^2))^2}{\sigma_{\text{tot}}^2} + \sum \ln(2\pi\sigma_{\text{tot}}^2) \quad , \quad (5)$$

where SF_{err}^2 represents the squared ensemble structure function due to magnitude measurement errors. Note that SF_{err}^2 depends upon L and λ (see the observed squared structure functions on short timescales in Figure 2). The variance

$\sigma_{\text{tot}}^2 = (c^2\sigma_{\text{SF}}^2 + \sigma_{\text{err}}^2)/(\ln(10) \times (c \times SF_{\text{mock}}^2 + SF_{\text{err}}^2))^2$, where σ_{SF}^2 and σ_{err}^2 represent the variance of SF_{mock}^2 and SF_{err}^2 , respectively. We then use *Scipy*’s optimization function to find the best-fitting parameters that minimizes

$$\chi_{\text{P}}^2 = \sum \chi_{\text{P,L},\lambda}^2 \quad . \quad (6)$$

There are sixteen free parameters: the first one is c , and the remaining fifteen ones are for SF_{err}^2 (five luminosity bins and three bands) which are well determined by SF_{obs}^2 on timescales of ≤ 4 days.

To measure the goodness of fit, we compute the two-sample Anderson-Darling test statistic (A_{obs}) between the observed and best-fitting mock squared structure functions for each luminosity bin and each band. We only use data points with $\Delta t > 10$ days since the structure functions are dominated by measurement errors on shorter timescales. Indeed, the squared ensemble structure functions on $\Delta t \lesssim 10$ days are larger than those on $\Delta t = 1$ day by a factor of $1.2 \sim 2.0$ (with a median value of 1.4), i.e., the intrinsic quasar squared ensemble structure functions are 20% \sim 100% of those due to measurement errors. Then, we adopt the “random subset selection” (RSS) method (which is widely used in the interpolated cross-correlation analysis) to assess the distribution of the statistic of the Anderson-Darling test. That is, we randomly select (with replacement) N data points from an observed structure function with N data points; only data points with unique Δt are used to construct a “fake” structure function; if the data point of the “fake” structure function is larger than ten, we apply the two-sample Anderson-Darling test to the observed and “fake” structure functions and store the corresponding statistic (A_{fake}). We repeat these procedures 10,000 times. For each luminosity bin at each band, we can obtain the NAAD of the Anderson-Darling test statistic (σ_{A}). The final statistic ($A_{\text{obs,tot}}$) between the best-fitting and observed structure functions for all luminosity bins and bands is the weighted average of A_{obs} in each luminosity bin and band and the weighting factor is $1/\sigma_{\text{A}}^2$. We can also obtain the corresponding fake total statistic ($A_{\text{fake,tot}}$), which is the weighted average of A_{fake} , for the 20,000 RSS simulations. If the best-fitting and observed structure functions are the same (the null hypothesis), we expect that the probability (p_{null}) for having $A_{\text{fake,tot}} \geq A_{\text{obs,tot}}$ in the 10,000 RSS simulations is not small. Given that we have 20,000 RSS simulations, if none of $A_{\text{fake,tot}}$ is larger than $A_{\text{obs,tot}}$, we can conclude that $p_{\text{null}} \lesssim 0.5/20000 = 2 \times 10^{-5}$. We reject models with $p_{\text{null}} < 0.05$ (i.e., $\log p_{\text{null}} < -1.3$).

4 RESULTS

We compare models with the same s and σ_{int} but different α . As an illustration, we fix $10^s = 500$ and $\sigma_{\text{int}} = 0.3 \text{ dex}^3$ and present the model squared structure functions with $\alpha = 0.2$ ($\alpha = 0.4$) in the upper (middle) rows of Figure 2. The model with $\alpha = 0.2$ fits the observed squared structure functions poorly and its p_{null} is much smaller than the alternative model with $\alpha = 0.4$. In fact, for all the 15 models with

¹ We also tried to set $\gamma = 0.6$ (e.g., [Aird et al. 2012](#)) and found that our conclusions remain largely unchanged.

² We confirm that our results remain the same if we use the luminosity-dependent bolometric correction factor.

³ The resulting M_{BH} distribution is close to [Kelly & Shen \(2013\)](#), who obtain their M_{BH} distribution by carefully correcting for biases in virial black-hole masses.

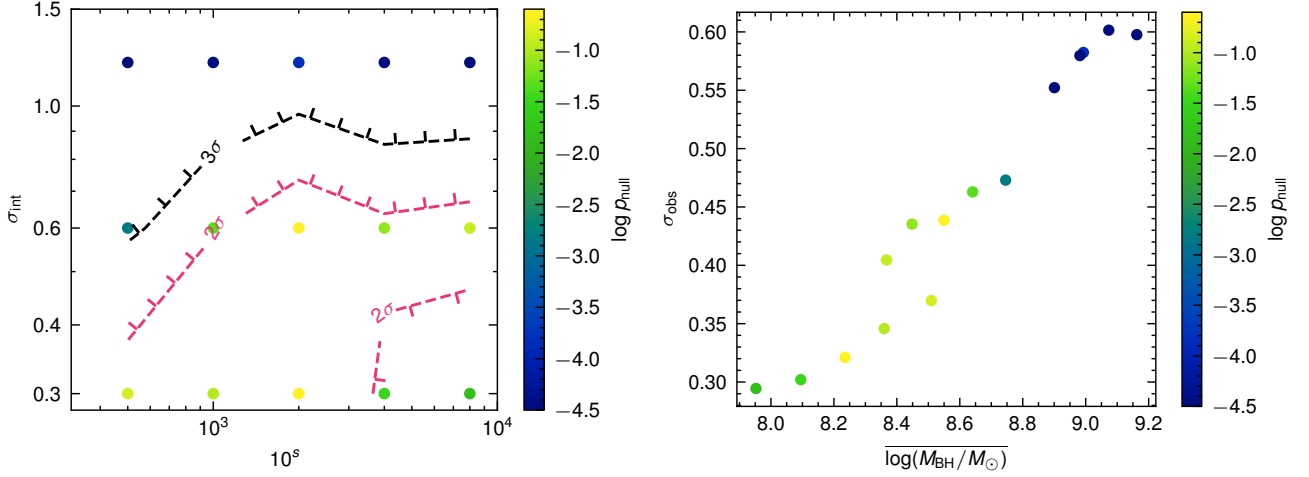


Figure 3. Left: the “allowed” normalization and intrinsic scatter of the $M_{\text{BH}} - M_*$ relation for $\alpha = 0.4$. The colours of data points correspond to the null hypothesis probability (i.e., if the model is true, the probability to generate the observed or even larger discrepancy between the data and the model prediction). The black and pink dashed curves indicate the parameter space with $\log p_{\text{null}} > -1.3$ (i.e., 2σ) and $\log p_{\text{null}} > -2.6$ (i.e., 3σ). No model has $\log p_{\text{null}} > -0.49$ (i.e., 1σ). Right: The average and NAAD of the M_{BH} distributions for mock quasars that are “detectable” (i.e., brighter than 20.34 mag in the i -band and have broad emission lines). Due to the selection effects, there is a clear correlation between the mean and NAAD of the mass distributions of the “detectable” mock quasars.

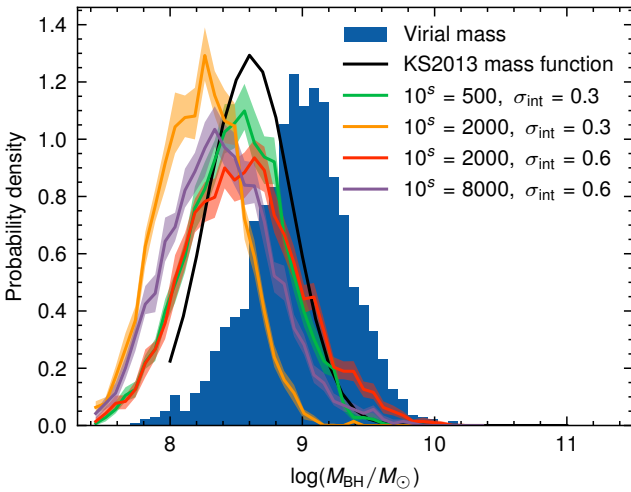


Figure 4. The distributions of $\log M_{\text{BH}}$ for the four cases with the highest p_{null} values (the green, yellow, red, and purple curves). The blue-shaded regions represent the distribution of the virial black-hole mass ($\log M_{\text{BH, vir}}$). The black curve shows the black-hole mass function of KS2013. Our $\log M_{\text{BH}}$ is, on average, smaller than $\log M_{\text{BH, vir}}$ by $0.3 \sim 0.6$ dex. The mean $\log M_{\text{BH}}$ values of the models with $[10^s = 500, \sigma_{\text{int}} = 0.3 \text{ dex}]$ and $[10^s = 2000, \sigma_{\text{int}} = 0.6 \text{ dex}]$ are slightly smaller than KS2013 by 0.12 dex and 0.06 dex, respectively.

$\alpha = 0.2$, their corresponding p_{null} are much smaller than 0.04% . Hence, the model squared structure functions with $\alpha = 0.2$ are statistically rejected for these luminous quasars (with $L_{\text{bol}} \gtrsim 10^{45.9} \text{ erg s}^{-1}$). In the subsequent analysis, we focus on models with $\alpha = 0.4$.

We can now compare model squared structure functions of various $\alpha = 0.4$ models with observed ones. The model and observed squared structure functions for $[10^s = 500,$

$\sigma_{\text{int}} = 0.3 \text{ dex}]$ and $[10^s = 500, \sigma_{\text{int}} = 1.2 \text{ dex}]$ (both with $\alpha = 0.4$) are presented in Figure 2. Unlike the latter model (with $p_{\text{null}} \lesssim 2 \times 10^{-5}$), the former one (with $p_{\text{null}} = 0.14$) is not statistically rejected by the observations, demonstrating the possibility to constrain M_{BH} distributions from quasar variability.

We can calculate the goodness of fit between the observed and model squared structure functions for different choices of s and σ_{int} which are the normalization and intrinsic scatter of the $M_{\text{BH}} - M_*$ relation, respectively. The results (corresponding to $\alpha = 0.4$) are presented in the left panel of Figure 3. Cases with $\sigma_{\text{int}} \geq 1.2$ dex have $\log p_{\text{null}} < -2.7$ (i.e., $p_{\text{null}} < 0.2\%$, which is smaller than the probability to be outside the 3σ regions of a Gaussian distribution) and are firmly rejected. Case 1 (i.e., $10^s = 500$ and $\sigma_{\text{int}} = 0.3$ dex) can explain the observed structure functions, which is consistent with recent results of the non-evolution of the $M_{\text{BH}} - M_*$ relation (e.g., Sun et al. 2015; Li et al. 2021). In the right panel of Figure 3, we plot the mean ($\overline{\log(M_{\text{BH}}/M_{\odot})}$) and NAAD (σ_{obs}) of the black-hole mass distributions of “detectable” mock quasars for all cases. Due to the selection effects (i.e., one can only detect luminous quasars), there is a clear correlation between $\overline{\log(M_{\text{BH}}/M_{\odot})}$ and σ_{obs} . The model squared structure functions of cases with $\overline{\log(M_{\text{BH}}/M_{\odot})} = 8.2 \sim 8.6$ and $\sigma_{\text{obs}} = 0.3 \sim 0.45$ dex are similar to the observed ones and have large p_{null} (the right panel of Figure 3).

We show the distributions of $\log M_{\text{BH}}$ for the four cases with highest p_{null} (see solid curves with shaded regions in Figure 4). Comparing with $\log M_{\text{BH, vir}}$, our $\log M_{\text{BH}}$ for the four cases are systematically smaller by $0.3 \sim 0.6$ dex.⁴ This sys-

⁴ In Sun et al. (2020), we successfully reproduce the observed ensemble structure functions of SDSS S82 light curves with the CHAR model and $M_{\text{BH, vir}}$. This is because the light curves used in Sun et al. (2020) only include SDSS S82 observations and are shorter than this work. The SDSS S82 light curves can only probe the ensemble structure functions on rest-frame timescales $\lesssim 500$

tematic offset likely resembles the systematic biases of virial black-hole mass as mentioned by (Shen & Kelly 2010, see their figure 2). Kelly & Shen (2013, hereafter KS2013) modelled these biases and inferred the bias-corrected $\log M_{\text{BH}}$ distribution from $\log M_{\text{BH, vir}}$ for SDSS detected quasars. The $\log M_{\text{BH}}$ distributions for the two cases with [$10^s = 500$, $\sigma_{\text{int}} = 0.3$ dex] and [$10^s = 2000$, $\sigma_{\text{int}} = 0.36$ dex] are on average smaller than KS2013 by only 0.12 dex or 0.06 dex, respectively. For the other two cases, the $\log M_{\text{BH}}$ distributions are on average smaller than that of KS2013 by no more than 0.4 dex. Hence, in our opinion, the inferred mass distribution is acceptable.

5 SUMMARY AND FUTURE PROSPECTS

In this work, we have demonstrated the possibility to infer the M_{BH} distribution of quasars by modelling their UV/optical multi-wavelength ensemble structure functions. Some of our M_{BH} distributions is roughly consistent with the previous study of Kelly & Shen (2013) that fully accounts for the statistical biases of $M_{\text{vir, BH}}$. Comparing with existing quasar M_{BH} measurement methods, our approach does not rely on the knowledge of the unknown BLR structure. Basing on several assumptions (i.e., all galaxies harbour AGNs, M_{BH} and M_* are correlated, and the distribution of M_* and AGN Eddington ratios follow the Schechter function; see Section 3), we have also constrained the normalization and intrinsic scatter of the possible correlation between M_{BH} and M_* at redshift $z \simeq 1.6$.

Compared with SDSS and Pan-STARRS, LSST can provide deeper (by 3 ~ 5 mag) and higher cadence time-domain surveys (e.g., Brandt et al. 2018). Hence, its data can extend our analysis to lower black-hole mass ranges. We can also explore complex models involving different Eddington ratio distributions, the black-hole mass distributions, and SMBH spins. The results can also be used to calibrate the virial black hole at various redshifts.

ACKNOWLEDGMENTS

We thank J.X. Wang and Y.Q. Xue for helpful discussion. We thank the anonymous referee for his/her helpful comments that improved the manuscript. M.Y.S. acknowledges support from the National Natural Science Foundation of China (NSFC-11973002), the Natural Science Foundation of Fujian Province of China (No. 2022J06002), and the China Manned Space Project grant (No. CMS-CSST-2021-A06 and CMS-CSST-2021-B11).

Funding for the SDSS and SDSS-II has been provided by the Alfred P. Sloan Foundation, the Participating Institutions, the National Science Foundation, the U.S. Department of Energy, the National Aeronautics and Space Administration, the Japanese Monbukagakusho, the Max Planck Society, and the Higher Education Funding Council for England. The SDSS website is <http://www.sdss.org/>.

days for quasars at $z = 1.6$. On such timescales, models with different M_{BH} have similar structure functions (see Figure 2). Hence, the SDSS S82 light curves are too short to constrain M_{BH} .

The SDSS is managed by the Astrophysical Research Consortium for the Participating Institutions. The Participating Institutions are the American Museum of Natural History, Astrophysical Institute Potsdam, University of Basel, University of Cambridge, Case Western Reserve University, University of Chicago, Drexel University, Fermilab, the Institute for Advanced Study, the Japan Participation Group, Johns Hopkins University, the Joint Institute for Nuclear Astrophysics, the Kavli Institute for Particle Astrophysics and Cosmology, the Korean Scientist Group, the Chinese Academy of Sciences (LAMOST), Los Alamos National Laboratory, the Max-Planck Institute for Astronomy (MPIA), the Max-Planck-Institute for Astrophysics (MPA), New Mexico State University, Ohio State University, University of Pittsburgh, University of Portsmouth, Princeton University, the United States Naval Observatory, and the University of Washington.

The Pan-STARRS1 Surveys (PS1) and the PS1 public science archive have been made possible through contributions by the Institute for Astronomy, the University of Hawaii, the Pan-STARRS Project Office, the Max-Planck Society and its participating institutes, the Max Planck Institute for Astronomy, Heidelberg and the Max Planck Institute for Extraterrestrial Physics, Garching, The Johns Hopkins University, Durham University, the University of Edinburgh, the Queen's University Belfast, the Harvard-Smithsonian Center for Astrophysics, the Las Cumbres Observatory Global Telescope Network Incorporated, the National Central University of Taiwan, the Space Telescope Science Institute, the National Aeronautics and Space Administration under Grant No. NNX08AR22G issued through the Planetary Science Division of the NASA Science Mission Directorate, the National Science Foundation Grant No. AST-1238877, the University of Maryland, Eotvos Lorand University (ELTE), the Los Alamos National Laboratory, and the Gordon and Betty Moore Foundation.

This work makes use of the following Python packages: Matplotlib (Hunter 2007), Numpy & Scipy (van der Walt, Colbert, & Varoquaux 2011) and pyLCSIM (Campana 2017).

DATA AVAILABILITY

The SDSS S82 light curves can be downloaded from https://faculty.washington.edu/ivezic/cmacleod/qso_dr7/Southern.html. The Pan-STARRS second data release site is <https://catalogs.mast.stsci.edu/panstarrs/>. The CHAR model light curves are available upon reasonable request.

REFERENCES

- Aird J., Coil A. L., Moustakas J., Blanton M. R., Burles S. M., Cool R. J., Eisenstein D. J., et al., 2012, *ApJ*, 746, 90. doi:10.1088/0004-637X/746/1/90
- Blandford R. D., McKee C. F., 1982, *ApJ*, 255, 419. doi:10.1086/159843
- Botte V., Ciroi S., Rafanelli P., Di Mille F., 2004, *AJ*, 127, 3168. doi:10.1086/420803
- Brandt W. N., Ni Q., Yang G., Anderson S. F., Assef R. J., Barth A. J., Bauer F. E., et al., 2018, arXiv, arXiv:1811.06542
- Burke C. J., Shen Y., Blaes O., Gammie C. F., Horne

- K., Jiang Y.-F., Liu X., et al., 2021, *Sci*, 373, 789. doi:10.1126/science.abg9933
- Campana R., 2017, *ascl.soft*. ascl:1708.016
- Chambers K. C., Magnier E. A., Metcalfe N., Flewelling H. A., Huber M. E., Waters C. Z., Denneau L., et al., 2016, *arXiv*, arXiv:1612.05560
- Du P., Lu K.-X., Zhang Z.-X., Huang Y.-K., Wang K., Hu C., Qiu J., et al., 2016, *ApJ*, 825, 126. doi:10.3847/0004-637X/825/2/126
- Ferrarese L., Merritt D., 2000, *ApJL*, 539, L9. doi:10.1086/312838
- Flewelling H. A., Magnier E. A., Chambers K. C., Heasley J. N., Holmberg C., Huber M. E., Sweeney W., et al., 2020, *ApJS*, 251, 7. doi:10.3847/1538-4365/abb82d
- Gebhardt K., Bender R., Bower G., Dressler A., Faber S. M., Filippenko A. V., Green R., et al., 2000, *ApJL*, 539, L13. doi:10.1086/312840
- Georgakakis A., Papadakis I., Paolillo M., 2021, *MNRAS*, 508, 3463. doi:10.1093/mnras/stab2818
- Homayouni Y., Trump J. R., Grier C. J., Horne K., Shen Y., Brandt W. N., Dawson K. S., et al., 2020, *ApJ*, 901, 55. doi:10.3847/1538-4357/ababa9
- Hunter J. D., 2007, *CSE*, 9, 90. doi:10.1109/MCSE.2007.55
- Jones M. L., Hickox R. C., Black C. S., Hainline K. N., DiPompeo M. A., Goulding A. D., 2016, *ApJ*, 826, 12. doi:10.3847/0004-637X/826/1/12
- Kelly B. C., Shen Y., 2013, *ApJ*, 764, 45. doi:10.1088/0004-637X/764/1/45
- Kelly B. C., Treu T., Malkan M., Pancoast A., Woo J.-H., 2013, *ApJ*, 779, 187. doi:10.1088/0004-637X/779/2/187
- King A. R., Pringle J. E., Livio M., 2007, *MNRAS*, 376, 1740. doi:10.1111/j.1365-2966.2007.11556.x
- Leja J., Speagle J. S., Johnson B. D., Conroy C., van Dokkum P., Franx M., 2020, *ApJ*, 893, 111. doi:10.3847/1538-4357/ab7e27
- Li J., Silverman J. D., Ding X., Strauss M. A., Goulding A., Schramm M., Yesuf H. M., et al., 2021, *ApJ*, 922, 142. doi:10.3847/1538-4357/ac2301
- Li S.-S., Yang S., Yang Z.-X., Chen Y.-J., Songsheng Y.-Y., Liu H.-Z., Du P., et al., 2021, *ApJ*, 920, 9. doi:10.3847/1538-4357/ac116e
- MacLeod C. L., Ivezić Ž., Sesar B., de Vries W., Kochanek C. S., Kelly B. C., Becker A. C., et al., 2012, *ApJ*, 753, 106. doi:10.1088/0004-637X/753/2/106
- McHardy I. M., Arévalo P., Uttley P., Papadakis I. E., Summons D. P., Brinkmann W., Page M. J., 2007, *MNRAS*, 382, 985. doi:10.1111/j.1365-2966.2007.12411.x
- Onken C. A., Ferrarese L., Merritt D., Peterson B. M., Pogge R. W., Vestergaard M., Wandel A., 2004, *ApJ*, 615, 645. doi:10.1086/424655
- Pancoast A., Brewer B. J., Treu T., Park D., Barth A. J., Bentz M. C., Woo J.-H., 2014, *MNRAS*, 445, 3073. doi:10.1093/mnras/stu1419
- Shen Y., 2013, *BASI*, 41, 61
- Shen Y., Kelly B. C., 2010, *ApJ*, 713, 41. doi:10.1088/0004-637X/713/1/41
- Shen Y., Richards G. T., Strauss M. A., Hall P. B., Schneider D. P., Snedden S., Bizyaev D., et al., 2011, *ApJS*, 194, 45. doi:10.1088/0067-0049/194/2/45
- Suberlak K. L., Ivezić Ž., MacLeod C., 2021, *ApJ*, 907, 96. doi:10.3847/1538-4357/abc698
- Sun M., Trump J. R., Brandt W. N., Luo B., Alexander D. M., Jahnke K., Rosario D. J., et al., 2015, *ApJ*, 802, 14. doi:10.1088/0004-637X/802/1/14
- Sun M., Xue Y., Brandt W. N., Gu W.-M., Trump J. R., Cai Z., He Z., et al., 2020, *ApJ*, 891, 178. doi:10.3847/1538-4357/ab789e
- Sun M., Xue Y., Guo H., Wang J., Brandt W. N., Trump J. R., He Z., et al., 2020, *ApJ*, 902, 7. doi:10.3847/1538-4357/abb1c4
- Thanjavur K., Ivezić Ž., Allam S. S., Tucker D. L., Smith J. A., Gwyn S., 2021, *MNRAS*, 505, 5941. doi:10.1093/mnras/stab1452
- Vanden Berk D. E., Richards G. T., Bauer A., Strauss M. A., Schneider D. P., Heckman T. M., York D. G., et al., 2001, *AJ*, 122, 549. doi:10.1086/321167
- van der Walt S., Colbert S. C., Varoquaux G., 2011, *CSE*, 13, 22. doi:10.1109/MCSE.2011.37
- Wu Q., Shen Y., 2022, *ApJS*, 263, 42. doi:10.3847/1538-4365/ac9ead
- Yu Z., Martini P., Penton A., Davis T. M., Kochanek C. S., Lewis G. F., Lidman C., et al., 2022, *arXiv*, arXiv:2208.05491
- Zhou X.-L., Zhang S.-N., Wang D.-X., Zhu L., 2010, *ApJ*, 710, 16. doi:10.1088/0004-637X/710/1/16

APPENDIX A

In this section, we illustrate our modelling results for other luminosity bins (Figures A5, A6, A7, and A8).

This paper has been typeset from a $\text{\TeX}/\text{\LaTeX}$ file prepared by the author.

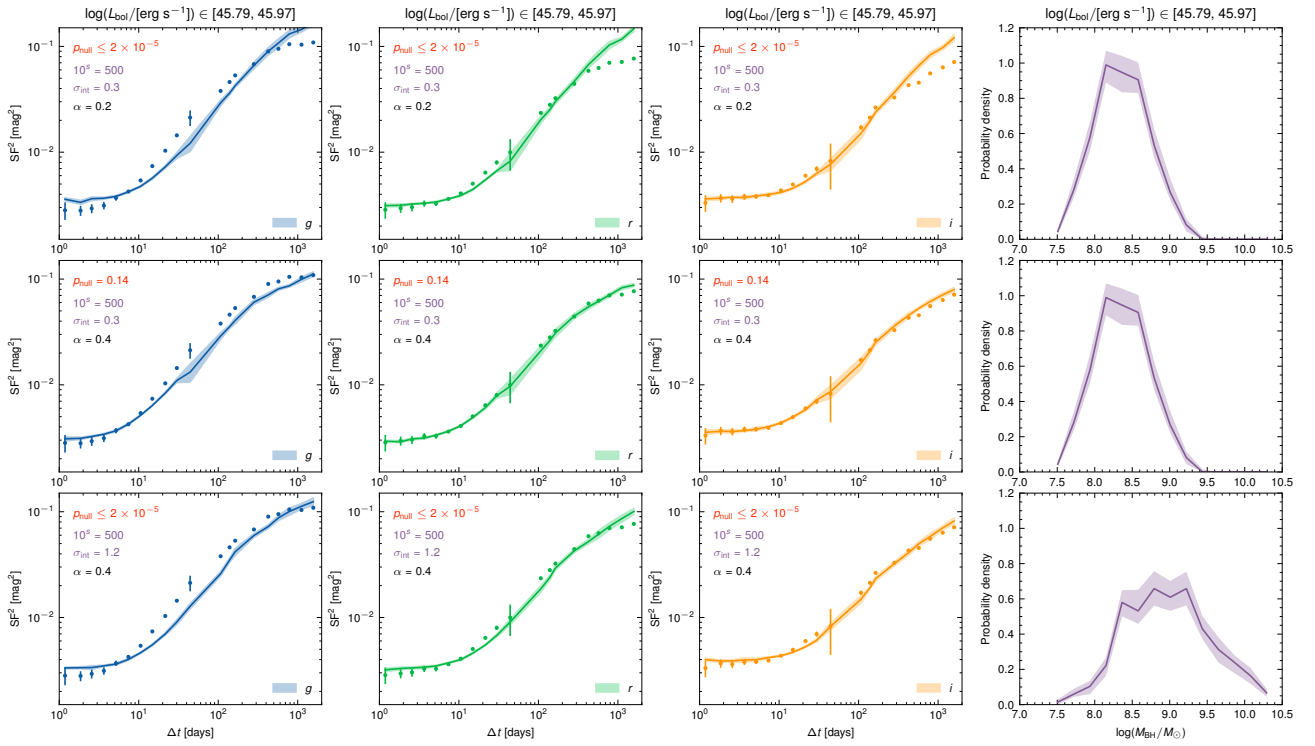


Figure A5. The same as Figure 2, but for the luminosity bin $45.79 \leq \log(L_{\text{bol}}/\text{erg s}^{-1}) < 45.97$.

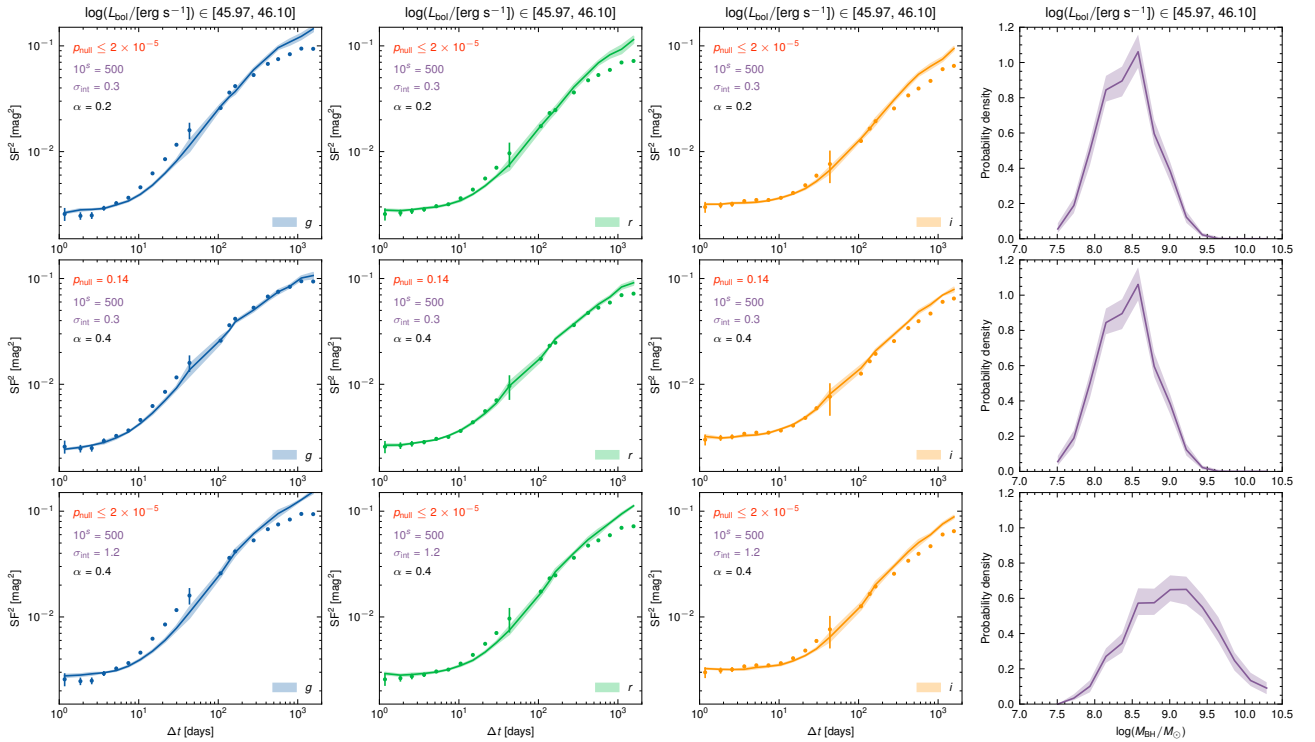


Figure A6. The same as Figure 2, but for the luminosity bin $45.97 \leq \log(L_{\text{bol}}/\text{erg s}^{-1}) < 46.10$.

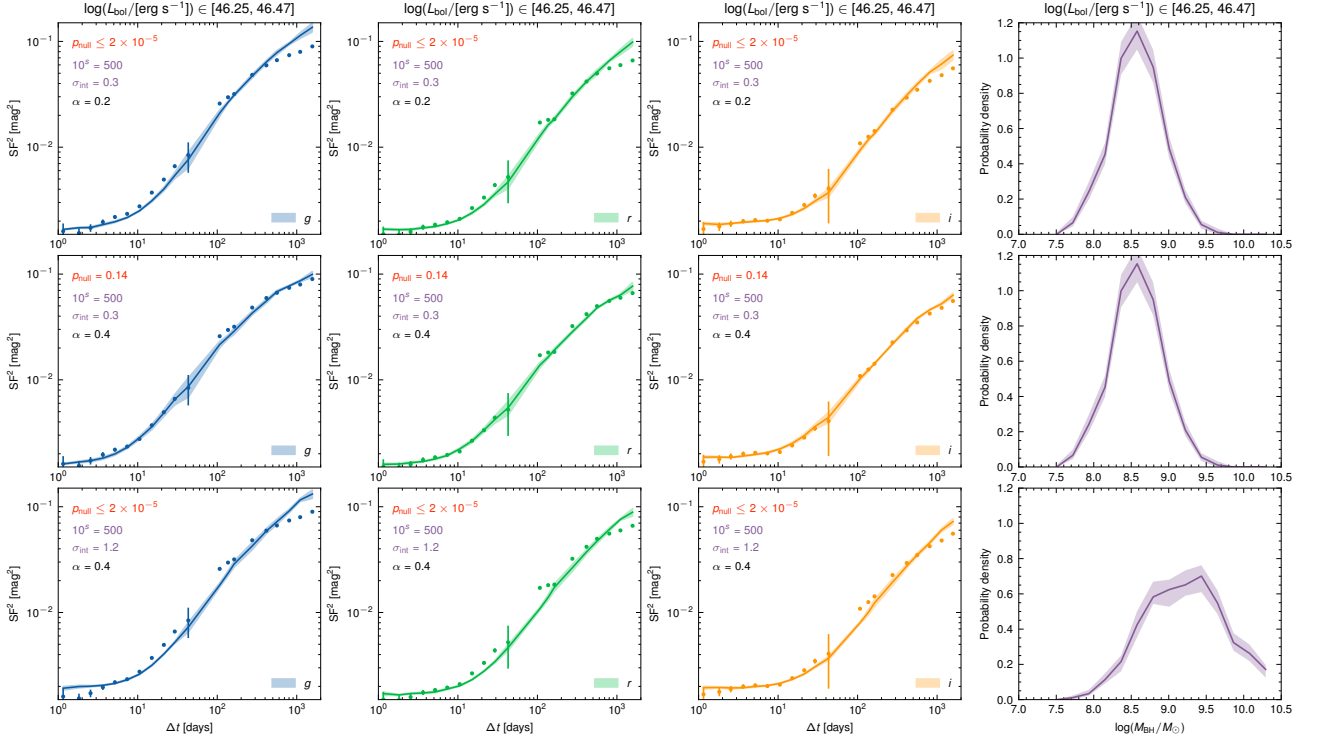


Figure A7. The same as Figure 2, but for the luminosity bin $46.25 \leq \log(L_{\text{bol}}/[\text{erg s}^{-1}]) < 46.47$.

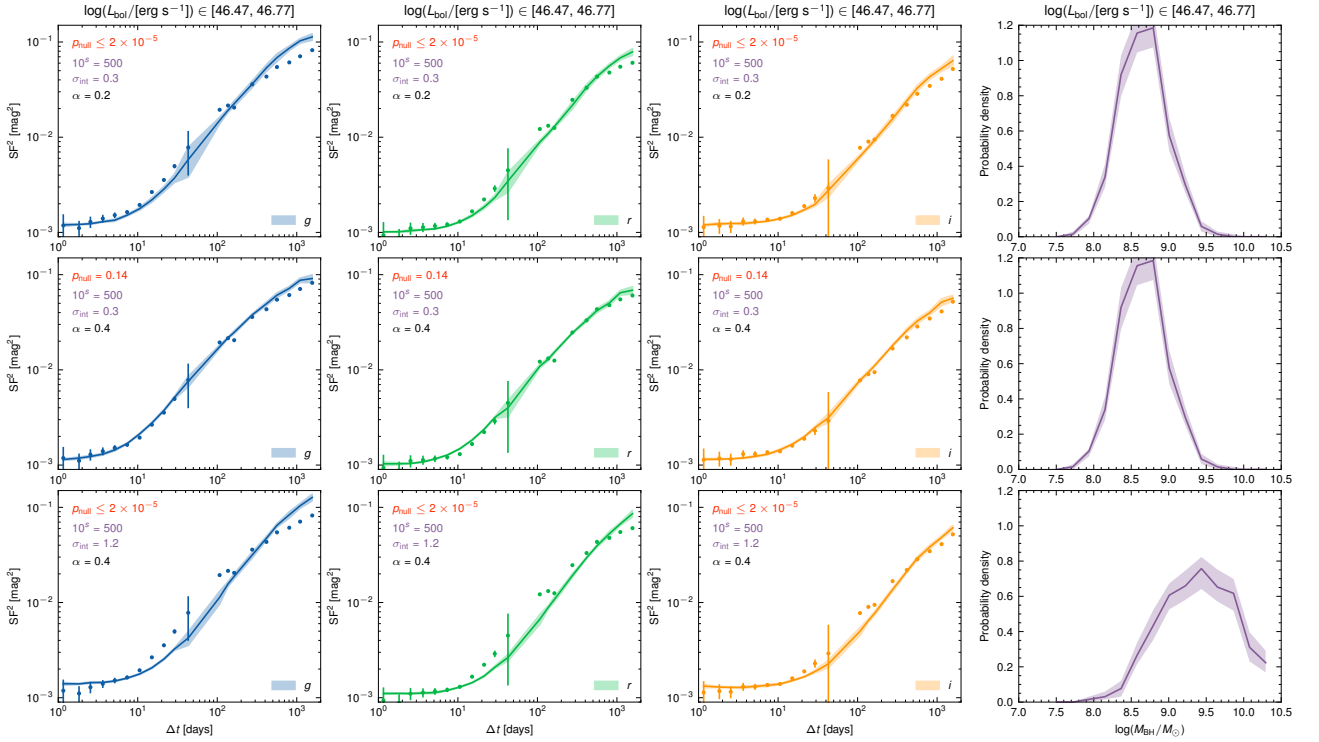


Figure A8. The same as Figure 2, but for the luminosity bin $46.47 \leq \log(L_{\text{bol}}/[\text{erg s}^{-1}]) < 46.77$.